Journal of Energy Chemistry 53 (2021) 132–138

Contents lists available at ScienceDirect

Journal of Energy Chemistry

journal homepage: www.elsevier.com/locate/jechem

http://www.journals.elsevier.com/journal-of-energy-chemistry/

Communication

Amorphous MoS_3 enriched with sulfur vacancies for efficient electrocatalytic nitrogen reduction

Ke Chu [a,*], Haifeng Nan [a], Qingqing Li [a], Yali Guo [a], Ye Tian [b], Wuming Liu [c]

[a] School of Materials Science and Engineering, Lanzhou Jiaotong University, Lanzhou 730070, Gansu, China
[b] Department of Physics, College of Science, Hebei North University, Zhangjiakou 075000, Hebei, China
[c] Institute of Physics, Chinese Academy of Sciences, Beijing 100190, China

ARTICLE INFO

Article history:
Received 1 April 2020
Revised 29 April 2020
Accepted 30 April 2020
Available online 19 May 2020

Keywords:
Electrocatalytic N_2 reduction
Amorphous materials
Vacancy
N_2 activation

ABSTRACT

Developing low-priced, yet effective and robust catalysts for the nitrogen reduction reaction (NRR) is of vital importance for scalable and renewable electrochemical NH_3 synthesis. Herein, we provide the first demonstration of MoS_3 as an efficient and durable NRR catalyst in neutral media. The prepared amorphous MoS_3 naturally possessed enriched S vacancies and delivered an NH_3 yield of 51.7 μg h^{-1} mg^{-1} and a Faradaic efficiency of 12.8% at −0.3 V (RHE) in 0.5 M $LiClO_4$, considerably exceeding those of MoS_2 and most reported NRR catalysts. Density functional theory calculations unraveled that S vacancies involved in MoS_3 played a crucial role in activating the NRR via a consecutive mechanism with a low energetics barrier and simultaneously suppressing the hydrogen evolution reaction.

Artificial N_2 fixation to NH_3 plays a crucial role in the human society, because NH_3 is a critical fertilizer precursor and also a promising carbon-free power source [1]. Nonetheless, the conventional NH_3 production is highly dependent on the Haber-Bosch process that is highly energy intensive and CO_2 emissive [2]. Ambient electrochemical N_2 reduction reaction (NRR) represents the most attractive alternative for renewable NH_3 synthesis [3–5]. Unfortunately, the efficiency of NRR process is largely prohibited by the poor N_2 polarization, large energetics barriers and great competitive hydrogen evolution reaction (HER) [6]. Therefore, it is critically important to design low-priced, yet active and stable electrocatalysts to facilitate the NRR and restrain the undesired HER. In recent years, intensive research has been triggered to develop a wide range of potential NRR catalysts, such as precious metals [7–10], earth-abundant metal compounds [11–17], and metal-free materials [18–21], with their performance further improved by manipulating size/phase [22–24], creating vacancies/strain [25–29], and introducing dopants/heterointerfaces [30–32].

Recent advance has shown that MoS_2 is a very promising NRR candidate attributed primarily to its active edge sites in facilitating the N_2 activation [33–35]. Nonetheless, the NRR performance of most existing MoS_2-based catalysts is still far less satisfactory due possibly to their limited available edges and poor intrinsic conductivity. MoS_3, possessing a disordered molecular-chain-like structure, is another type of important molybdenum sulfide material [36]. MoS_3 has recently emerged as a fascinating catalyst for electrocatalytic reactions by virtue of its special structural/physical advantages, including amorphous nature, high S concentration and good conductivity. These advantages of MoS_3 are also highly attractive for the NRR because: (1) amorphous structure of MoS_3 contains abundant unsaturated coordination sites and surface-exposed defects which provide plentiful active sites to capture and activate the inert N_2 molecule [37]; (2) higher S concentration of MoS_3 than MoS_2 favors the creation of more S vacancies that are conductive to the effective N_2 adsorption/activation [30]. (3) MoS_3 possesses a higher intrinsic conductivity than MoS_2 due to its smaller band gap [38], which is advantageous to the NRR kinetics by accelerating the electron transfer efficiency [22]. These distinct merits demonstrate the great promise of MoS_3 as an efficient NRR catalyst, which, however, has not been studied thus far.

Herein, we report MoS_3 as an effective and stable electrocatalyst for the NRR. The prepared amorphous MoS_3 naturally contained rich S vacancies and exhibited an NH_3 yield of 51.7 μg h^{-1} mg^{-1} and a Faradaic efficiency (FE) of 12.8% at −0.3 V (RHE) in 0.5 M $LiClO_4$, dramatically outperforming the crystalline MoS_2. Density functional theory (DFT) calculations unveiled that S vacancies involved in MoS_3 acted as the catalytic centers to effectively activate N_2 and boost the NRR energetics.

* Corresponding author.
E-mail address: chukelut@163.com (K. Chu).

https://doi.org/10.1016/j.jechem.2020.04.074

The sheet-like MoS_3 was prepared through the liquid exfoliation of bulk MoS_3, and the preparation details are given in the Experimental Section (Supporting Information). As shown in Fig. 1(a), the X-ray diffraction (XRD) pattern of MoS_3 shows no diffraction peaks, suggesting the amorphous phase of MoS_3. X-ray photoelectron spectroscopy (XPS) is used to examine the surface chemical states of MoS_3. The deconvoluted Mo 3*d* spectra (Fig. 1(b)) reveal three well-resolved peaks of S2s (225.9 eV), Mo^{6+} $3d_{5/2}$ (228.7 eV) and Mo^{6+} $3d_{3/2}$ (232.2 eV). The deconvoluted S 2*p* spectra (Fig. 1(c)) show two doublets, corresponding to terminal (161.8, 162.7 eV) and bridging (163.5, 164.8 eV) sulfide ligands (S_2^{2-}/S^{2-}), coinciding well with those of reported MoS_3 [36]. The transmission electron microscopy (TEM, Fig. 1(d)) image of MoS_3 presents the morphology of interconnected porous nanosheets. Such porous nanostructure can also be reflected by the nitrogen adsorption–desorption measurement (Fig. S1), showing a large specific surface area (123.7 m^2 g^{-1}) together with the abundant mesopores (centered at 10–20 nm), which facilitate the electrochemical reactions by providing more catalytically active sites and sufficient reactant/ion transport. Also, a halo feature can be observed in the selected area electron diffraction (SAED, Fig. 1(d), inset) pattern of MoS_3, confirming the amorphous structure of MoS_3.

Scanning TEM (STEM, Fig. 1(e)) analysis of MoS_3 presents the uniform distribution of Mo and S elements. The S/Mo molar ratio is determined to be 2.71 by inductively coupled plasma atomic emission spectrometry (ICP-AES), suggesting the existence of rich S vacancies in MoS_3. Furthermore, in the high-resolution TEM (HRTEM) image of MoS_3 (Fig. 1(f)), two randomly selected regions (labeled as 1 and 2) are analyzed by the Fourier transform (FFT) and corresponding inverse FFT (IFFT) techniques [39–43], which reveal the sun-like pattern (FFT, top) and highly disordered lattice fringes (IFFT, bottom), further testifying the amorphous feature of MoS_3, which shows the disordered molecular-chain-like structure, as illustrated in Fig. 1(g). All these characterizations prove the successful synthesis of amorphous MoS_3.

As illustrated in Fig. 2(a), after thermal annealing amorphous MoS_3 at 600 °C for 3 h under argon atmosphere, the crystalline MoS_2 can be obtained, which can be verified by the following characterizations. After annealing, the XRD pattern (Fig. 2(b)) shows the appeared peaks that can be well indexed to 2H-MoS_2 (JCPDS No.87–1536). The XPS S 2*p* spectra (Fig. 2(c)) show fitted S $2p_{3/2}$ (162.3 eV) and S $2p_{1/2}$ (163.5 eV) of 2H-MoS_2, which differ significantly from the S 2*p* spectra of MoS_3. The SAED pattern (Fig. 2(d), inset) displays the clear diffraction rings that are well assigned to (002), (100) and (110) facets of 2H-MoS_2 (Fig. S2). The HRTEM image (Fig. 2(e)) presents the clear lattice fringes with an interplanar distance of 0.62 nm, assigned to (002) facet of 2H-MoS_2. Furthermore, as depicted in Fig. 2(f), the electron paramagnetic resonance (EPR) spectra reveal that MoS_3 shows a much stronger

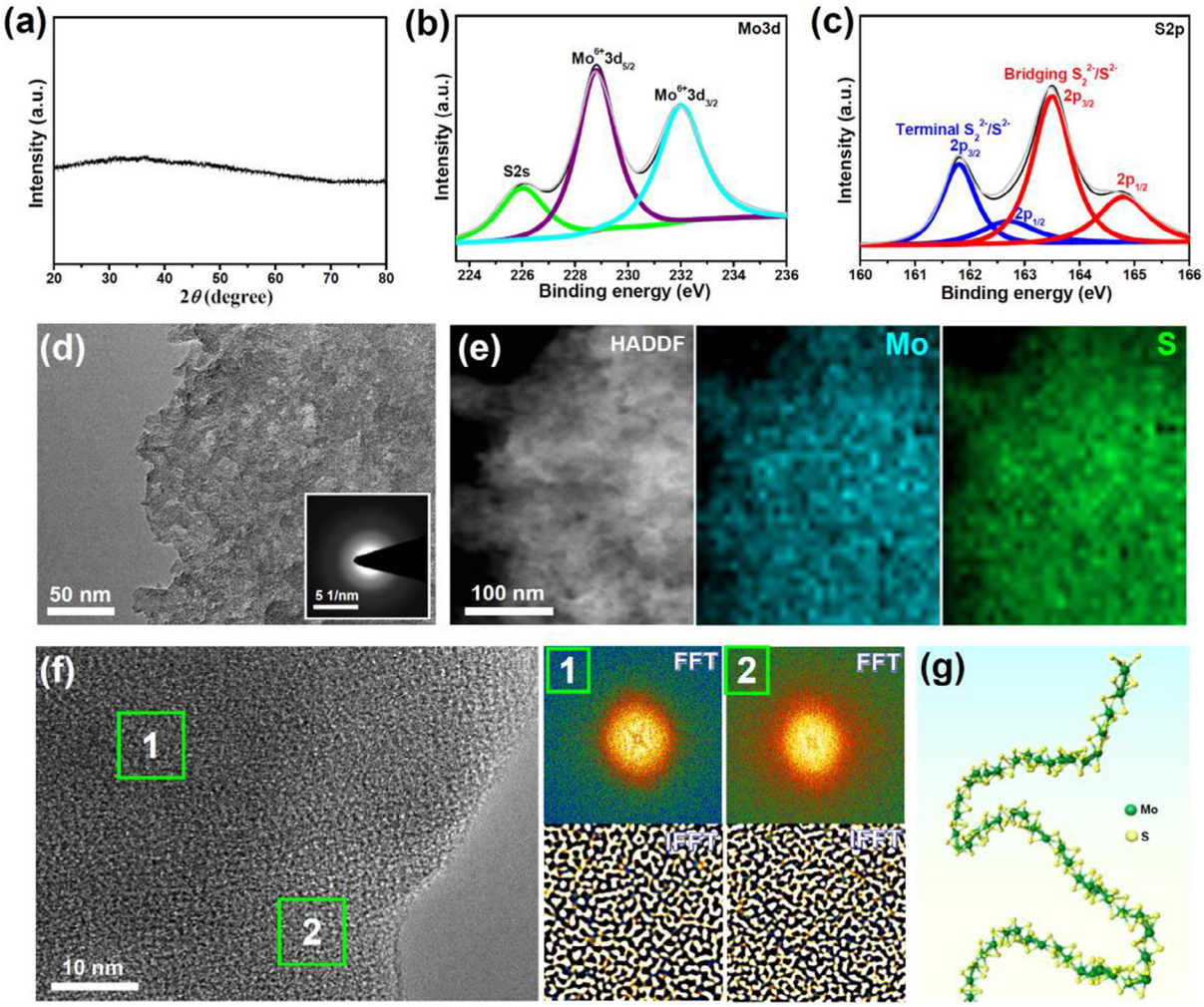

Fig. 1. Characterization of as-prepared MoS_3: (a) XRD pattern; (b) XPS Mo 3*d* spectra; (c) S 2*p* spectra; (d) TEM image (inset: SAED pattern); (e) STEM element mapping images; (f) HRTEM image and corresponding FFT/IFFT analysis selected in the regions of 1 and 2; (g) Schematic of the disordered molecular-chain-like structure of MoS_3.

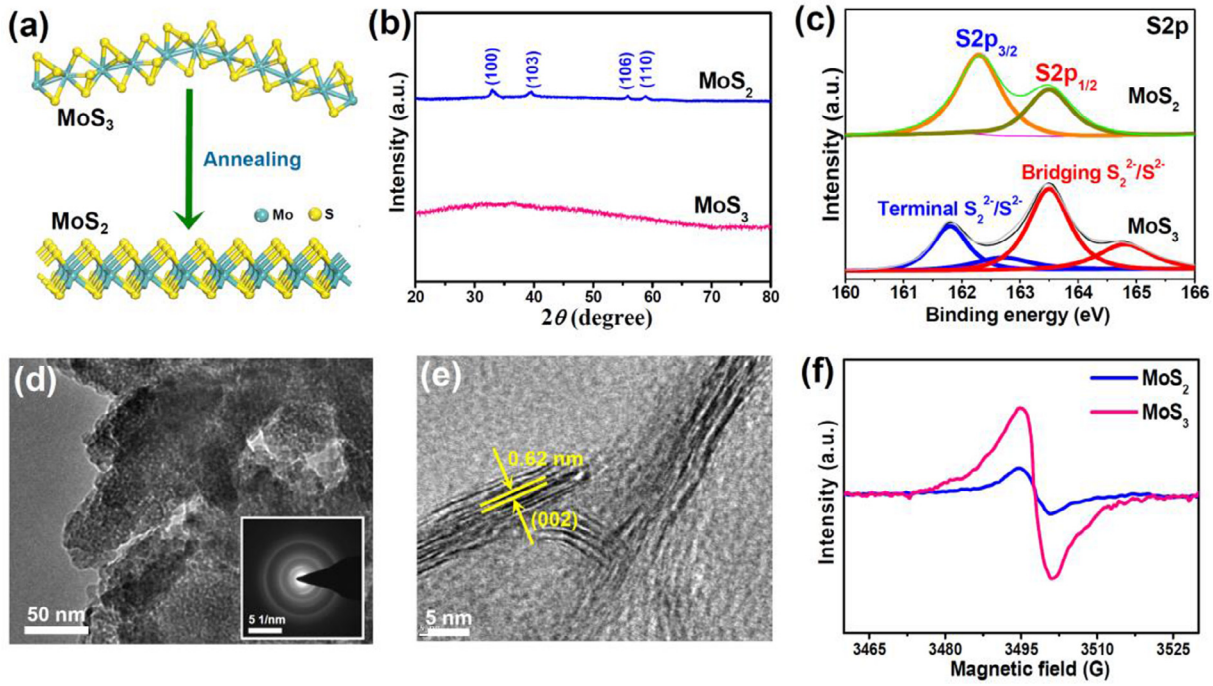

Fig. 2. (a) Schematic of the phase transformation from amorphous MoS_3 to crystalline MoS_2. (b) XRD patterns of MoS_2 and MoS_3; (c) XPS S 2*p* spectra of MoS_2 and MoS_3; (d) TEM image of MoS_2 (inset: SAED pattern); (e) HRTEM image of MoS_2; (f) EPR spectra of MoS_2 and MoS_3.

EPR signal intensity than MoS_2. This suggests that MoS_3 naturally possesses a high concentration of S vacancies and most of vacancies would be vanished during the conversion of amorphous MoS_3 to crystalline MoS_2. The enriched S vacancies involved in MoS_3 are expected to remarkably promote the NRR activity owing to the strong electron-donating effect of vacancy to favorably transfer the electrons into the $2\pi^*$ antibonding orbitals of N_2 molecule for N_2 activation [30,31].

The catalytic NRR performance of MoS_3 deposited on carbon cloth (CC) was assessed in 0.5 M $LiClO_4$ using a gas-tight H-type cell [44]. A selection of $LiClO_4$ as the NRR electrolyte is two-fold: 1) it is extensively used for NRR reaction [45–47]. 2) Li^+ ions can, to some extent, retard the HER process by virtue of Li-O or Li-S interactions in hindering H^+ adsorption and H_2 evolution [35,48]. As shown in the linear scan voltammetry curves of MoS_3 (Fig. S3), an noticeably increased current density can be seen in N_2-saturated with respect to Ar-saturated electrolyte in the potential range of −0.2 – −0.6 V, which indicates the occurrence of NRR over MoS_3 in such potential window [16]. The chronoamperometry tests were combined with the colorimetric measurements to quantitatively evaluate the NRR performance of MoS_3 [49,50]. The reductive products including NH_3 and possible N_2H_4 were analyzed by the colorimetric methods, and their calibration curves are presented in Figs. S4 and S5. After electrolysis over MoS_3 from −0.2 to −0.6 V (Fig. 3(a)), the produced NH_3 was determined by the UV–vis absorption spectra, and corresponding data of NH_3 yield and FE are shown in Fig. 3(b). Clearly, MoS_3 exhibits the optimum NRR performance at −0.3 V, achieving the highest NH_3 yield of 51.7 μg h^{-1} mg^{-1} (10.3 μg cm^{-2} h^{-1}) and FE of 12.8%, which exceed those of most reported electrocatalysts (Table S1). Nonetheless, with increasing the potential over −0.3 V, a sharp decline can be found for both NH_3 yield and FE, which is due primarily to the enhanced HER to restrict the NRR [51]. Moreover, as shown in Fig. S6, the N_2H_4 as a by-product is undetectable, which means a high NRR selectivity of MoS_3.

To get further insight into the NRR activity of MoS_3, the NRR performance of comparative MoS_2 is also considered (Fig. S7). As presented in Fig. 3(c), MoS_2 presents the much unsatisfactory NRR performance with the optimum NH_3 yield (11.3 μg h^{-1} mg^{-1}) and FE (3.9%) to be 4.6 times and 3.3 times poorer than those of MoS_3, respectively. To uncover the significant NRR enhancement in MoS_3 as compared to MoS_2, we conduct the double-layer capacitance (C_{dl}), dinitrogen temperature-programmed desorption (N_2-TPD) and electrochemical impedance spectroscopy (EIS) measurements. The C_{dl} test (Fig. 3(d) & Fig. S8) shows that MoS_3 (6.5 mF cm^{-2}) possesses a nearly twice larger C_{dl} than MoS_2 (3.4 mF cm^{-2}), indicating a higher concentration of catalytically active sites in MoS_3, which is attributed to the amorphous structure of MoS_3 enriched with S vacancies (Fig. 2(f)), as well as the porous nanostructure of MoS_3 with large surface area (Fig. S1) [52–54]. Specifically, the abundant S vacancies involved in MoS_3 can act as trapping sites for effectively capturing and adsorbing N_2 [27], as evidenced by the N_2-TPD test (Fig. 3(e)) showing a more positive and stronger chemical desorption peak for MoS_3 with respect to MoS_2. Additionally, EIS test (Fig. 3(f)) indicates that MoS_3 presents a smaller charge resistance than MoS_2, suggesting the enhanced charge transfer efficiency and boosted electrocatalytic kinetics of MoS_3. Therefore, in comparison with crystalline MoS_2, the amorphous MoS_3 with rich S vacancies exhibits improved N_2 chemisorption and accelerated electron transfer, engendering the greatly promoted NRR performance.

To testify the reliable NRR experiments, the control tests were performed to exclude the possible interferences from any environmental N-containing contaminants. Isotopic labelling experiment is carried out to trace the origin of N source [55], as shown in Fig. 4(a). After electrolysis over MoS_3 using $^{15}N_2$ or $^{14}N_2$ as feed gas, ^1H nuclear magnetic resonance (NMR) spectra present a distinguished doublet for $^{15}NH_4^+$ (*J*-coupling: ~72 Hz) when using $^{15}N_2$, or a triplet for $^{14}NH_4^+$ (*J*-coupling: ~52 Hz) when using $^{14}N_2$. No labeled $^{15}NH_4^+$ and $^{14}NH_4^+$ can be detected when using Ar as feed gas,

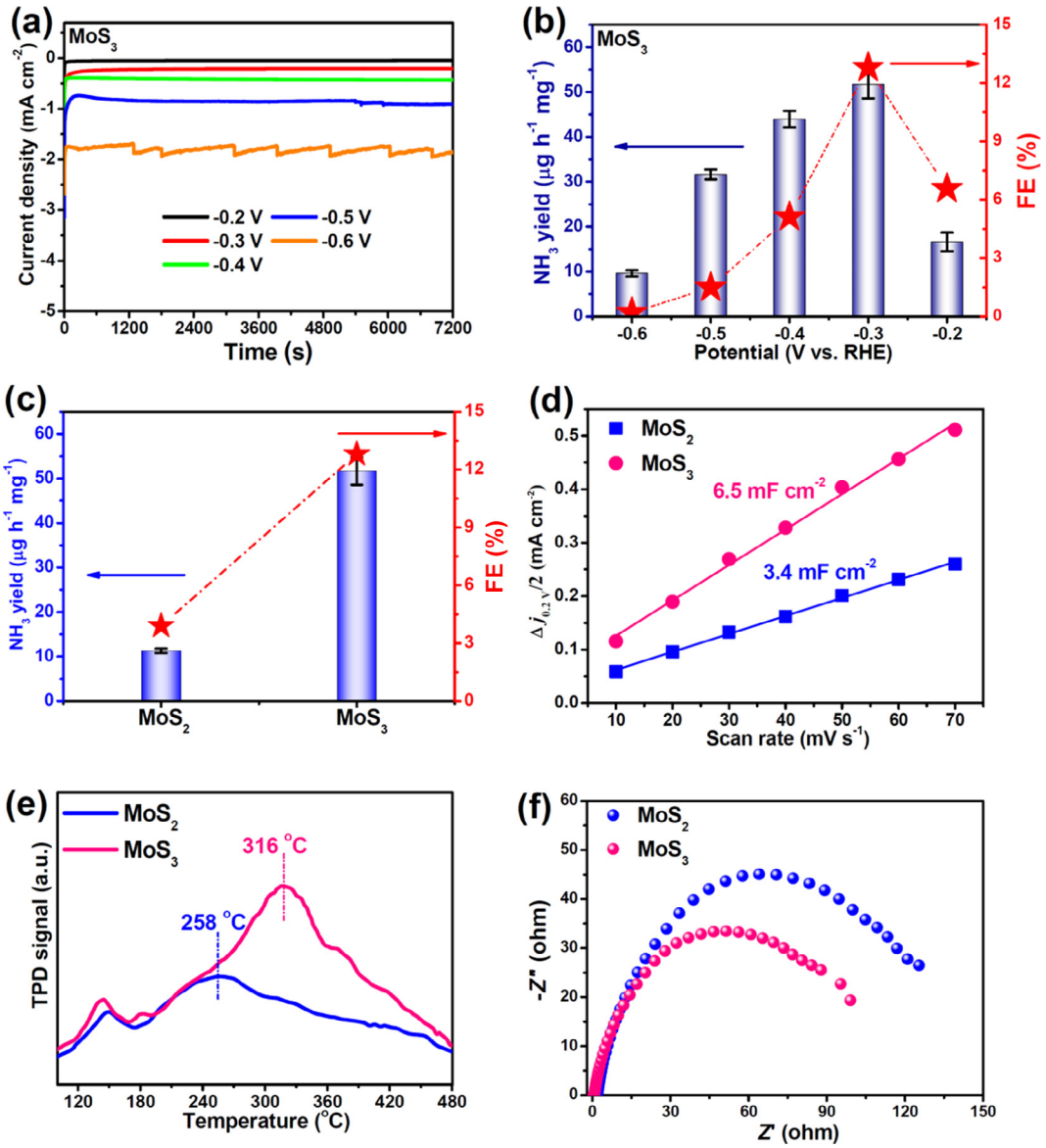

Fig. 3. (a) Chronoamperometry test of MoS_3 for 2 h of NRR electrolysis at various potentials, and (b) corresponding NH_3 yields and FEs. (c) Comparison of the optimum NH_3 yields and FEs of MoS_2 and MoS_3. (d) double-layer capacitance (C_{dl}) measurements of MoS_2 and MoS_3. (e) N_2-TPD spectra of MoS_2 and MoS_3. (f) Electrochemical impendence spectra of MoS_2 and MoS_3.

indicating that the detected $^{15}NH_4^+$ and $^{14}NH_4^+$ are derived from the NRR [56–58]. In addition, the control tests in terms of colorimetric measurements (Fig. S9) do not generate a detectable amount of NH_3 [59]. Thus, we can surely confirm that the generated NH_3 definitely derives from the NRR rather than from unnoticed contaminations.

We further assess the NRR durability of MoS_3. When performing seven chronoamperometric runs (Fig. 4(b)), it is seen in Fig. 4(c) that MoS_3 displays small fluctuates in the values of NH_3 yield and FE, suggesting the good cycling stability [60,61]. MoS_3 also possesses the excellent long-term operation durability, as evidenced by the negligible loss of the current density for 20 h of continuous electrolysis (Fig. 4(d)). Furthermore, MoS_3 still retains its amorphous structure (Fig. 4(e and f)), porous nanosheet morphology (Fig. S10) and chemical bonding states (Fig. S11), confirming the stable structure of MoS_3 for the NRR. Therefore, the high NRR activity and robust durability demonstrate that present MoS_3 is a promising catalyst candidate for the N_2 electroreduction.

DFT calculation was performed to establish a basic understanding for the high NRR activity of MoS_3. To simulate the molecular-chain-like structure of MoS_3, we build one-dimensional Mo_6S_{18} cluster model consisting of six MoS_3 units, as illustrated in Fig. S12. To begin with, we consider the N_2 adsorption which is the prerequisite step to initialize the NRR [62–64]. As seen in Fig. 5(a), the absorbed N_2 molecule can not form the bond with the surface atom(s) of MoS_3, resulting in nearly unchanged N≡N bond and negligible charge transfer, thus making pristine MoS_3 catalytically inactive for NRR.

When a surface S vacancy (V_s) is introduced in MoS_3 (MoS_3-V_s), N_2 can be well fixed into the V_s position of MoS_3-V_s through either end-on (Fig. 5(b)) or side-on (Fig. 5(c)) pattern, indicating that V_s plays a critical role in polarizing the inert N_2. The higher degree of N≡N bond elongation and electron donation for side-on adsorption (1.176 Å, −0.38 |e|) as compared to end-on adsorption (1.147 Å, −0.25 |e|) suggests that N_2 adsorption preferentially occurs via side-on configuration. For side-on pattern, after initial hydrogenation by adding one H atom (Fig. 5(d)), the N≡N triple bond can be cleaved into the N = N double bond with the bond lengthen further stretched to 1.289 Å, indicating that MoS_3-V_s

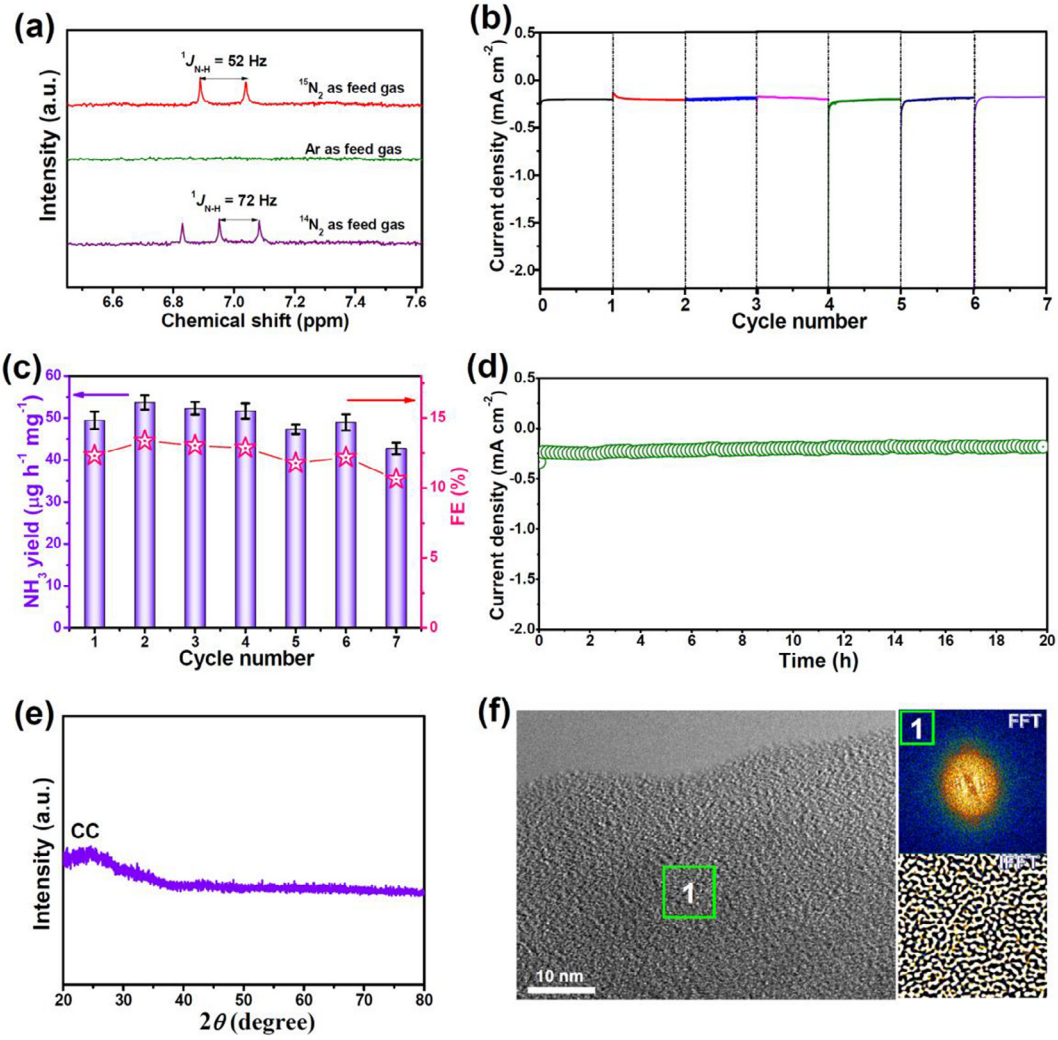

Fig. 4. (a) ^{1}H NMR measurements over MoS_3 using $^{14}N_2$, $^{15}N_2$ and Ar as feed gases. (b) Chronoamperometry tests of MoS_3 for seven cycles, and obtained (c) NH_3 yields and FEs. (d) Chronoamperometry test of MoS_3 for 20 h of NRR electrolysis at −0.3 V. (e) XRD and (f) HRTEM image (FFT/IFFT recorded in 1 region) of MoS_3 after the stability test.

can effectively activate N_2 to promote the N≡N bond dissociation and hydrogenation reaction.

We then move on to assess the energetics of MoS_3-V_s by constructing the Gibbs free energy diagrams (Fig. 5(f)) via two possible associative hydrogenation pathways, including enzymatic and consecutive (similar to distal mechanism but through side-on pattern [30]) mechanisms, with their optimized atom configurations of the reaction intermediates shown in Fig. 5(e). For the enzymatic pathway, the rate-determining step (RDS) is *NH–*NH → *NH–*NH_2 with the highest energy barrier (ΔG_{RDS}) of 1.07 eV, whereas the most difficult step for consecutive pathway is the initial hydrogenation of *N_2 → *N-*NH with the ΔG_{RDS} considerably reduced to 0.58 eV. Thus, the hydrogenation of MoS_3-V_s prefers to undergo through consecutive pathway rather than enzymatic pathway. In general, the scaling relation exists in the electrocatalytic NRR process [65], that is, the strong N_2 adsorption/activation to lower the initial hydrogenation barrier may cause the excessive binding of certain NRR intermediates to largely increase the energy barrier of following reaction steps. Accordingly, such scaling relation works well for the enzymatic pathway by substantially lifting the energy barrier of *NH–*NH → *NH–*NH_2 due to the excessive binding of *NH–*NH, whereas the consecutive pathway can weaken the scaling relation to favorably balance the binding energies of NRR intermediates, eventually resulting in reduced energetic barrier and more preferred NRR process. We further calculate the overpotential η of MoS_3-V_s on the basis of $\eta = U_e - U_L$ [66], where U_e is the equilibrium potential of NRR (−0.16 V) and U_L is the limiting potential ($U_L = -\Delta G_{PDS}/e = -0.58$ V). The calculated η is 0.42 V for MoS_3-V_s, which is theoretically lower than those of most reported MoS_2-based NRR electrocatalysts, such as MoS_2 (0.71 V [32]), defect-rich MoS_2 (0.44 V) [33], MoS_2/C_3N_4 heterostructure (0.46 V) [32], and Co-doped MoS_2 (0.78 V) [67], suggesting the great promise of MoS_3-V_s for the NRR.

We finally sought to examine whether NRR-efficient MoS_3-V_s is also active for the HER. In general, HER involves a two-step process in neutral or alkaline electrolyte: water dissociation and then hydrogen evolution [44]. An efficient HER catalyst should possess low water dissociation energy (ΔG_{H2O}) and have a nearly zero *H adsorption energy (ΔG_{*H}). As presented in Fig. 5(g), albeit MoS_3-V_s favors the H_2 evolution with a relatively low ΔG_{*H} (−0.32 eV), it possesses a highly positive ΔG_{H2O} (0.97 eV), which inhibits the initial cleavage of H-OH bond and limits the overall HER kinetics. We also find that ΔG_{*N2} (−0.47 eV) is more negative than ΔG_{*H} (−0.32 eV), suggesting the preferential adsorption of N_2 rather than H^+ on MoS_3-V_s in the catalytic reactions, which is more likely to facilitate the NRR and restrict the HER. Therefore, MoS_3-V_s can effectively suppress the HER and activate the NRR in neutral electrolyte, agreeing well with the favorable NRR performance of MoS_3 determined in the experiments.

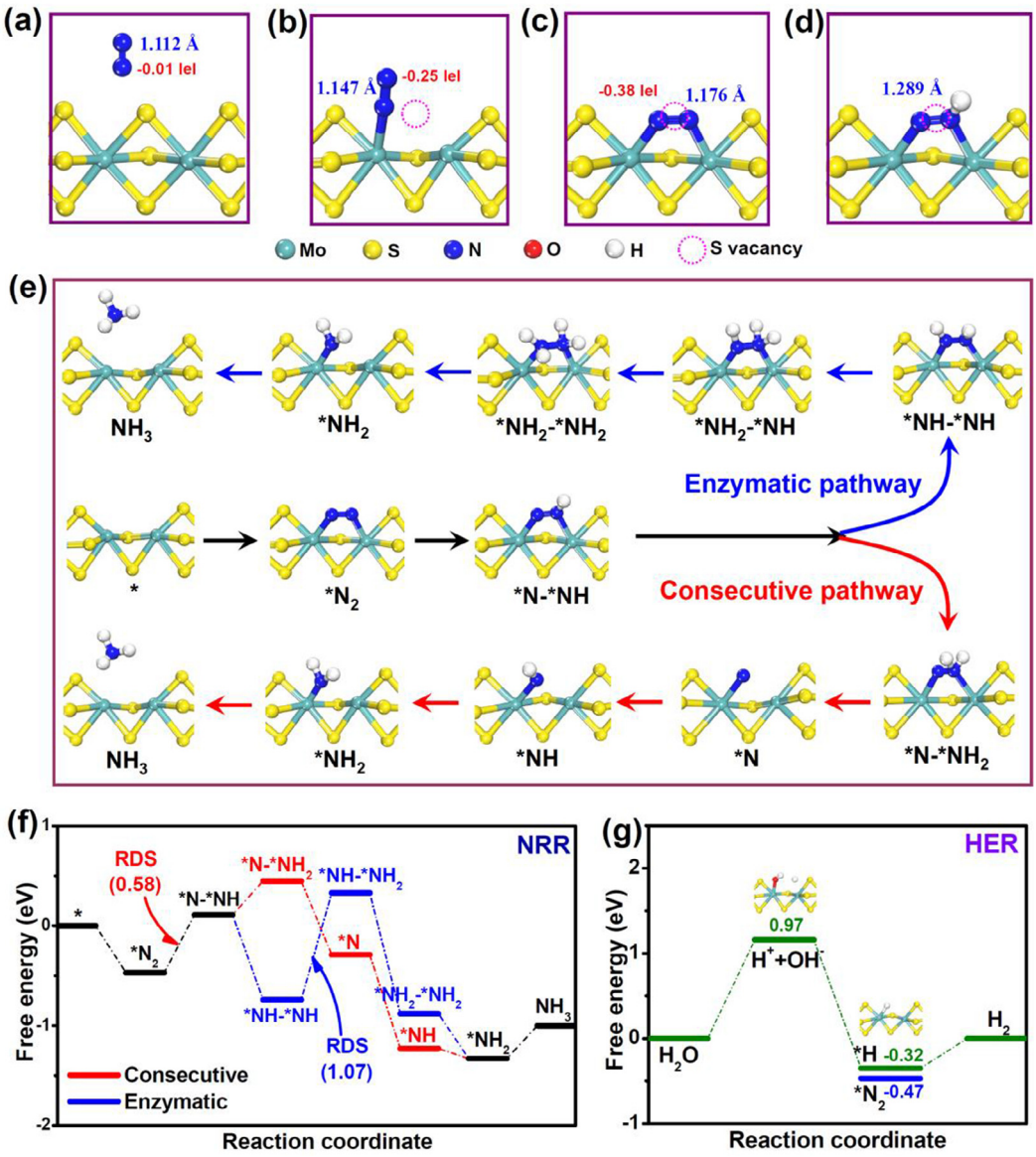

Fig. 5. (a–c) Optimized structures of $^*N_2$ over (a) pristine MoS_3, (b, c) MoS_3 with a surface V_s (MoS_3-V_s. b: end-on pattern, c: side-on pattern). (d) Optimized structures of $^*N$-$^*NH$ over MoS_3-V_s. (e) Schematic of the NRR pathways over MoS_3-V_s. (f) Free energy diagrams of NRR pathways over MoS_3-V_s at zero potential. (g) Free energy diagram of HER pathway over MoS_3-V_s in neutral media.

In summary, a combination of experimental methodology and computational calculations validated that amorphous MoS_3 enriched with S vacancies could be a highly efficient NRR catalyst with an NH_3 yield of 51.7 μg h^{-1} mg^{-1} and an FE of 12.8% at −0.3 V in 0.5 M $LiClO_4$, together with the outstanding long-term durability. DFT analysis unveiled that S vacancies involved in MoS_3 served as the catalytic centers that could effectively activate N_2, reduce the energetics barrier through a consecutive mechanism, and concurrently inhibit the HER. These findings suggest the promising potential of MoS_3 and related materials for application in electrochemical N_2 fixation to NH_3.

Declaration of Competing Interest

The authors declare that they have no known competing financial interests or personal relationships that could have appeared to influence the work reported in this paper.

Acknowledgments

This work is supported by the National Natural Science Foundation of China (51761024), the CAS "Light of West China" Program, "Feitian Scholar" Program of Gansu Province, and the Foundation of A Hundred Youth Talents Training Program of Lanzhou Jiaotong University.

Appendix A. Supplementary data

Supplementary data to this article can be found online at https://doi.org/10.1016/j.jechem.2020.04.074.

References

[1] J.A. Brandes, N.Z. Boctor, G.D. Cody, B.A. Cooper, R.M. Hazen, H.S. Yoder Jr, Nature 395 (1998) 365.

[2] T. Kandemir, M.E. Schuster, A. Senyshyn, M. Behrens, R. Schlögl, Angew. Chem. Int. Edit. 52 (2013) 12723–12726.
[3] X. Cui, C. Tang, Q. Zhang, Adv. Energy. Mater. 8 (2018) 1800369.
[4] X. Zhu, S. Mou, Q. Peng, Q. Liu, Y. Luo, G. Chen, S. Gao, X. Sun, J. Mater. Chem. A 8 (2020) 1545–1556.
[5] Y. Yang, Y. Tang, H. Jiang, Y. Chen, P. Wan, M. Fan, R. Zhang, S. Ullah, L. Pan, J.-J. Zou, M. Lao, W. Sun, C. Yang, G. Zheng, Q. Peng, T. Wang, Y. Luo, X. Sun, A.S. Konev, O.V. Levin, P. Lianos, H. Zhuofeng, Z. Shen, Q. Zhao, Y. Wang, N. Todorova, C. Trapalis, M.V. Sheridan, H. Wang, L. Zhang, S. Sun, W. Wang, J. Ma, Chinese Chem. Lett. 30 (2019) 2089–2109.
[6] G.F. Chen, S.Y. Ren, L.L. Zhang, H. Cheng, Y.R. Luo, K.H. Zhu, L.X. Ding, H.H. Wang, Small Methods 3 (2019) 1800337.
[7] H. Xie, Q. Geng, X. Zhu, Y. Luo, L. Chang, X. Niu, X. Shi, A.M. Asiri, S. Gao, Z. Wang, X. Sun, J. Mater. Chem. A 7 (2019) 24760–24764.
[8] R. Zhao, C. Liu, X. Zhang, X. Zhu, P. Wei, L. Ji, Y. Guo, S. Gao, Y. Luo, Z. Wang, X. Sun, J. Mater. Chem. A 8 (2020) 77–81.
[9] Y. Yang, S.-Q. Wang, H. Wen, T. Ye, J. Chen, C.-P. Li, M. Du, Angew. Chem. Int. Edit. 131 (2019) 15506–15510.
[10] G. Deng, T. Wang, A.A. Alshehri, K.A. Alzahrani, Y. Wang, H. Ye, Y. Luo, X. Sun, J. Mater. Chem. A 7 (2019) 21674–21677.
[11] Q. Liu, R. Zhang, H. Guo, L. Yang, Y. Wang, Z. Niu, H. Huang, H. Chen, L. Xia, T. Li, Chem. Electro. Chem. 6 (2019) 1014–1018.
[12] J. Yu, C. Li, B. Li, X. Zhu, R. Zhang, L. Ji, D. Tang, A.M. Asiri, X. Sun, Q. Li, S. Liu, Y. Luo, Chem. Commun. 55 (2019) 6401–6404.
[13] H. Jin, L. Li, X. Liu, C. Tang, W. Xu, S. Chen, L. Song, Y. Zheng, S.-Z. Qiao, Adv. Mater. 31 (2019) 1902709.
[14] H. Cheng, L.X. Ding, G.F. Chen, L.L. Zhang, J. Xue, H.H. Wang, Adv. Mater. 30 (2018) 1803694.
[15] G. Yu, H. Guo, S. Liu, L. Chen, A.A. Alshehri, K.A. Alzahrani, F. Hao, T. Li, A.C.S. Appl, Mater. Inter. 11 (2019) 35764–35769.
[16] H. Xian, H. Guo, Z. Chen, G. Yu, A.A. Alshehri, K.A. Alzahrani, F. Hao, R. Song, T. Li, A.C.S. Appl, Mater. Inter. 12 (2020) 2445–2451.
[17] T. Wu, W. Kong, Y. Zhang, Z. Xing, J. Zhao, T. Wang, X. Shi, Y. Luo, X. Sun, Small Methods (2019) 1900356.
[18] X. Zhu, T. Wu, L. Ji, C. Li, T. Wang, S. Wen, S. Gao, X. Shi, Y. Luo, Q. Peng, X. Sun, J. Mater. Chem. A 7 (2019) 16117–16121.
[19] L. Xia, X. Wu, Y. Wang, Z. Niu, Q. Liu, T. Li, X. Shi, A.M. Asiri, X. Sun, Small Methods 3 (2018) 1800251.
[20] X. Yu, P. Han, Z. Wei, L. Huang, Z. Gu, S. Peng, J. Ma, G. Zheng, Joule 2 (2018) 1610–1622.
[21] L. Xia, J. Yang, H. Wang, R. Zhao, H. Chen, W. Fang, A.M. Asiri, F. Xie, G. Cui, X. Sun, Chem. Commun. 55 (2019) 3371–3374.
[22] K. Chu, Y. Liu, Y. Li, J. Wang, H. Zhang, ACS Appl. Mater. Inter. 11 (2019) (1815) 31806–31813.
[23] Y.P. Liu, Y.B. Li, D.J. Huang, H. Zhang, K. Chu, Chem. Eur. J. 25 (2019) (1939) 11933–11941.
[24] K. Chu, Y. Cheng, Q. Li, Y. Liu, Y. Tian, J. Mater. Chem. A 8 (2020) 5865–5873.
[25] Y.B. Li, Y.P. Liu, J. Wang, Y.L. Guo, K. Chu, Inorg. Chem. Front. 7 (2020) 455–463.
[26] L. Zhang, X.-Y. Xie, H. Wang, L. Ji, Y. Zhang, H. Chen, T. Li, Y. Luo, G. Cui, X. Sun, Chem. Commun. 55 (2019) 4627–4630.
[27] G. Zhang, Q. Ji, K. Zhang, Y. Chen, Z. Li, H. Liu, J. Li, J. Qu, Nano Energy 59 (2019) 10–16.
[28] S. Cheng, Y.-J. Gao, Y.-L. Yan, X. Gao, S.-H. Zhang, G.-L. Zhuang, S.-W. Deng, Z.-Z. Wei, X. Zhong, J.-G. Wang, J. Energy Chem. 39 (2019) 144–151.
[29] X. Tang, Z. Wei, Q. Liu, J. Ma, J. Energy Chem. 33 (2019) 155–159.
[30] K. Chu, J. Wang, Y.P. Liu, Q.Q. Li, Y.L. Guo, J. Mater. Chem. A 8 (2020) 7117–7124.
[31] K. Chu, Y. Liu, Y. Chen, Q. Li, J. Mater. Chem. A 8 (2020) 5200–5208.
[32] K. Chu, Y.P. Liu, Y.B. Li, Y.L. Guo, Y. Tian, A.C.S. Appl, Mater. Inter. 12 (2020) 7081–7090.
[33] X. Li, T. Li, Y. Ma, Q. Wei, W. Qiu, H. Guo, X. Shi, P. Zhang, A.M. Asiri, L. Chen, B. Tang, X. Sun, Adv. Energy. Mater. 8 (2018) 1801357.
[34] L. Zhang, X. Ji, X. Ren, Y. Ma, X. Shi, Z. Tian, A.M. Asiri, L. Chen, B. Tang, X. Sun, Adv. Mater. 30 (2018) 1800191.
[35] Y. Liu, M. Han, Q. Xiong, S. Zhang, C. Zhao, W. Gong, G. Wang, H. Zhang, H. Zhao, Adv. Energy. Mater. 9 (2019) 1803935.
[36] H. Ye, L. Wang, S. Deng, X. Zeng, K. Nie, P.N. Duchesne, B. Wang, S. Liu, J. Zhou, F. Zhao, N. Han, P. Zhang, J. Zhong, X. Sun, Y. Li, Y. Li, J. Lu, Adv. Energy. Mater. 7 (2017) 1601602.
[37] C. Lv, C. Yan, G. Chen, Y. Ding, J. Sun, Y. Zhou, G. Yu, Angew. Chem. Int. Edit. 57 (2018) 6073–6076.
[38] Y. Pan, W. Guan, J. Power Sources 325 (2016) 246–251.
[39] K. Chu, F. Wang, Y.B. Li, X.H. Wang, D.J. Huang, Z.R. Geng, Compos. Part A 109 (2018) 267–279.
[40] K. Chu, J. Wang, Y.P. Liu, Y.B. Li, C.C. Jia, H. Zhang, Carbon 143 (2019) 85–96.
[41] K. Chu, F. Wang, X.H. Wang, Y.B. Li, Z.R. Geng, D.J. Huang, H. Zhang, Mater. Design 144 (2018) 290–303.
[42] K. Chu, F. Wang, Y.B. Li, X.H. Wang, D.J. Huang, H. Zhang, Carbon 133 (2018) 127–139.
[43] K. Chu, F. Wang, X.H. Wang, D.J. Huang, Mater. Sci. Eng. A 713 (2018) 269–277.
[44] K. Chu, Q. Li, Y. Liu, J. Wang, Y. Cheng, Appl. Catal. B 267 (2020) 118693.
[45] Y. Li, Q. Zhang, C. Li, H.-N. Fan, W.-B. Luo, H.-K. Liu, S.-X. Dou, J. Mater. Chem. A 7 (2019) 22242–22247.
[46] Y. Song, D. Johnson, R. Peng, D.K. Hensley, P.V. Bonnesen, L. Liang, J. Huang, F. Yang, F. Zhang, R. Qiao, Sci. Adv. 4 (2018) e1700336.
[47] T. Wu, Z. Xing, S. Mou, C. Li, Y. Qiao, Q. Liu, X. Zhu, Y. Luo, X. Shi, Y. Zhang, X. Sun, Angew. Chem. Int. Edit. 58 (2019) 18449–18453.
[48] G.F. Chen, X.R. Cao, S.Q. Wu, X.Y. Zeng, L.X. Ding, M. Zhu, H.H. Wang, J. Am. Chem. Soc. 139 (2017) 9771–9774.
[49] J. Wang, Y.P. Liu, H. Zhang, D.J. Huang, K. Chu, Catal. Sci. Technol. 9 (2019) 4248–4254.
[50] Y.P. Liu, Y.B. Li, H. Zhang, K. Chu, Inorg. Chem. 58 (2019) 10424–10431.
[51] P. Wang, Q.Q. Li, Y.H. Cheng, K. Chu, J. Mater. Sci. 55 (2020) 4624–4632.
[52] K. Chu, X.H. Wang, F. Wang, Y.B. Li, D.J. Huang, H. Liu, W.L. Ma, F.X. Liu, H. Zhang, Carbon 127 (2018) 102–112.
[53] K. Chu, X.H. Wang, Y.B. Li, D.J. Huang, Z.R. Geng, X.L. Zhao, H. Liu, H. Zhang, Mater. Design 140 (2018) 85–94.
[54] K. Chu, J. Wang, Y.P. Liu, Z.R. Geng, Carbon 140 (2018) 112–123.
[55] S.Z. Andersen, V. Čolić, S. Yang, J.A. Schwalbe, A.C. Nielander, J.M. McEnaney, K. Enemark-Rasmussen, J.G. Baker, A.R. Singh, B.A. Rohr, M.J. Statt, S.J. Blair, S. Mezzavilla, J. Kibsgaard, P.C.K. Vesborg, M. Cargnello, S.F. Bent, T.F. Jaramillo, I. E.L. Stephens, J.K. Nørskov, I. Chorkendorff, Nature 570 (2019) 504–508.
[56] K. Chu, Q.Q. Li, Y.H. Cheng, Y.P. Liu, ACS Appl. Mater. Inter. 12 (2020) 11789–11796.
[57] X.H. Wang, J. Wang, Y.B. Li, K. Chu, Chem. Cat. Chem. 11 (2019) 4529–4536.
[58] K. Chu, Y. Liu, J. Wang, H. Zhang, A.C.S. Appl, Energy Mater. 2 (2019) 2288–2295.
[59] K. Chu, Y. Liu, Y. Li, H. Zhang, Y. Tian, J. Mater. Chem. A 7 (2019) 4389–4394.
[60] H. Xian, Q. Wang, G. Yu, H. Wang, Y. Li, Y. Wang, T. Li, Appl. Catal. A 581 (2019) 116–122.
[61] F. Wang, Y.P. Liu, H. Zhang, K. Chu, Chem. Cat. Chem. 11 (2019) 1441–1447.
[62] Z. Wei, Y. Feng, J. Ma, J. Energy Chem. 48 (2020) 322–327.
[63] Z. Wei, Y. Zhang, S. Wang, C. Wang, J. Ma, J. Mater. Chem. A 6 (2018) 13790–13796.
[64] C. Liu, Q. Li, C. Wu, J. Zhang, Y. Jin, D.R. MacFarlane, C. Sun, J. Am. Chem. Soc. 141 (2019) 2884–2888.
[65] E. Skúlason, T. Bligaard, S. Gudmundsdóttir, F. Studt, J. Rossmeisl, F. Abild-Pedersen, T. Vegge, H. Jónsson, J.K. Nørskov, Phys. Chem. Chem. Phys. 14 (2012) 1235–1245.
[66] K. Chu, Y. Liu, Y. Li, Y. Guo, Y. Tian, H. Zhang, Appl. Catal. B 264 (2020) 118525.
[67] J. Zhang, X. Tian, M. Liu, H. Guo, J. Zhou, Q. Fang, Z. Liu, Q. Wu, J. Lou, J. Am. Chem. Soc. 141 (2019) 19269–19275.